AIAA JOURNAL
Vol. 33, No. 9, September 1995

Pressure-Based Control-Volume Finite Element Method for Flow at All Speeds

S. M. H. Karimian* and G. E. Schneider†
University of Waterloo, Waterloo, Ontario N2L 3G1, Canada

This paper presents a collocated pressure-based method for the solution of viscous/inviscid fluid flow problems incorporating compressible and incompressible regimes. The solution domain is discretized using a control-volume-based finite element method. The fully implicit method does not experience any stability difficulties due to compressibility effects at low Mach numbers. The pressure/velocity decoupling problem is fully resolved herein for flow regimes from incompressible through compressible flow. Transonic and supersonic flows are covered by including the pressure/density coupling, which arises in high-speed flows, in the continuity equation. This is done in such a manner that the continuity equation remains a constraint equation for pressure in all flow regimes. Test problems with wide variations in geometry and fluid physics have been successfully solved, demonstrating the generality and computational capability of the method. The scheme is both efficient and robust. The accuracy of the method has been checked by comparing the results with other numerical results available in the literature and with the exact solution.

Nomenclature

C_p, C_v	= specific heats
$\hat{E}, \hat{F}$	= convection flux vectors
e	= total energy per unit mass
$\hat{G}, \hat{H}$	= diffusion flux vectors
h	= total enthalpy per unit mass
L	= distance between up and dn
M	= Mach number
$N_i(\hat{s}, \hat{t})$	= shape function
P	= nodal pressure
p	= pressure
$\hat{Q}$	= conserved quantity vector
q	= velocity magnitude
R	= gas constant
S	= source
s	= local streamwise direction
$\hat{s}, \hat{t}$	= local coordinates
T	= nodal temperature
t	= temperature
t	= time
U, V	= nodal velocity components
u, v	= velocity components
$\tilde{u}, \tilde{v}$	= streamwise interpolated velocity components
$\hat{u}, \hat{v}$	= convecting velocity components
$\boldsymbol{V}$	= velocity vector
x, y	= global coordinates
Γ	= general diffusion coefficient
ΔS	= distance between up and ip
$\Delta\phi$	= streamwise correction term for ϕ
$\Delta\rho$	= streamwise correction term for ρ
ρ	= density
ϕ	= arbitrary scalar

Subscripts

dn	= downstream
in	= inlet
ip	= integration point
up	= upstream

Superscripts

l	= approximated using bilinear interpolation
T	= transpose
$-$	= lagged value from the previous iteration

Presented as Paper 94-1960 at the AIAA/ASME 6th Joint Thermophysics and Heat Transfer Conference, Colorado Springs, CO, June 20–23, 1994; received July 19, 1994; revision received Feb. 21, 1995; accepted for publication March 4, 1995.

*Postdoctoral Research Fellow, Department of Mechanical Engineering. Member AIAA.

†Professor, Department of Mechanical Engineering. Associate Fellow AIAA.

Introduction

TODAY, a variety of computational methods for the solution of flow at all speeds can be found in the literature. These methods fall into two categories: 1) methods for compressible flow, extended to cover incompressible flow, and 2) methods for incompressible flow, extended to cover compressible flow. These methods work more efficiently in their original flow regime.

In the first category are time-marching methods that choose density, rather than pressure, as a primary variable. In low-Mach-number flow the time-dependent equations become "stiff." This results in both inefficiency and inaccuracy. To avoid these difficulties, different variants of preconditioning have been proposed. Turkle[1] suggested a preconditioning method by introducing an artificial time derivative of pressure in the continuity and momentum equations; see also Ref. 2. In the preconditioning procedure of Choi and Merkle[3] for inviscid flow, only the energy equation was modified by adding the time derivatives of ρ, ρu, and ρv. Choi and Merkle[4] improved their preconditioning method to include viscous flow calculations, using a set of primitive variable unknowns (P, u, v, T). Primitive variable unknowns also have been employed, in time-marching methods, by other investigators.[5] In the method of Pletcher and Chen,[6] a preconditioning procedure is applied to unsteady problems. The hyperbolic system of equations is iterated in pseudotime until the steady solution is reached at each physical time step.

In the finite element context, several methods have been presented for compressible flow calculations; see Refs. 7 and 8. Extensions of the streamline-upwinding/Petrov–Galerkin finite element method for compressible Euler and Navier–Stokes equations can also be found in the literature.[9,10] For the calculation of both compressible and incompressible flows, a semi-implicit finite element algorithm was proposed by Zienkiewicz et al.,[11] with extension to a general explicit/semi-explicit method by Zienkiewicz and Wu.[12]

The second category includes pressure-based methods that treat the continuity equation as a constraint equation for pressure rather than a time evolution equation for density. Using a staggered grid arrangement some of these methods, well established for

incompressible viscous flow,[13,14] have been extended to compressible flow.[15–17] Other methods in this category use a collocated grid. In these methods all of the variables are located at the nodal points. Different approaches[18–21] have been employed to resolve the pressure checkerboard problem. The objective of these methods is to bring the coupling between velocity and pressure into the continuity equation. Extensions of these methods for solving compressible flow can be found in the literature.[20,22]

In the collocated-variable method of Karimian and Schneider[23] for one-dimensional flow, a new formulation was introduced to remove the pressure checkerboard problem. The successful performance of this formulation in two-dimensional incompressible flow[21] led to the present study to develop a method for calculation of two-dimensional viscous/inviscid flow problems encompassing incompressible to supersonic regimes. The pressure/density coupling in high-speed flow is incorporated in the continuity equation, consistent with the pressure/velocity coupling in incompressible flow. The basic elements of the flow calculation are discussed, and numerical results are presented to demonstrate the method.

Domain Discretization and the Assembly Procedure

The solution domain is divided into quadrilateral elements. All of the problem unknowns including velocity components, pressure, and temperature are located at each node. The local coordinates $(\hat{s}, \hat{t})$ and local node numbers for a single element are shown in Fig. 1. Having defined x_i and y_i to be the global coordinates at local node i, the coordinate variation within the element is described by

$$x(\hat{s}, \hat{t}) = \sum_{i=1}^{4} N_i(\hat{s}, \hat{t})x_i \tag{1}$$

$$y(\hat{s}, \hat{t}) = \sum_{i=1}^{4} N_i(\hat{s}, \hat{t})y_i \tag{2}$$

where the bilinear shape functions $N_i(\hat{s}, \hat{t})$ are given by

$$N_i(\hat{s}, \hat{t}) = \tfrac{1}{4}(1 + \hat{s}_i\hat{s})(1 + \hat{t}_i\hat{t}) \qquad i = 1, 4 \tag{3}$$

in which $\hat{s}_i$ and $\hat{t}_i$ are defined in Fig. 1. The lines $\hat{s} = 0$ and $\hat{t} = 0$ divide each element into four quadrants, called subcontrol volumes (SCV), each associated with a node as shown in Fig. 2a. The SCVs surrounding a node define a control volume for the given node, as shown in Fig. 2b. For each element, a matrix equation, called the elemental matrix equation, is constructed. This elemental matrix equation is determined by applying mass, momentum, and energy conservation equations to each SCV within the element and will include a set of 16 equations for 16 unknowns for each element. Through the element assembly procedure, the SCV equations associated with a node are assembled to form the control-volume conservation equations of mass, momentum, and energy for the respective node.[19]

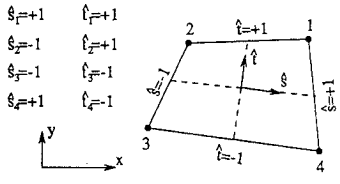

Fig. 1 Single element with local coordinates and local node numbers.

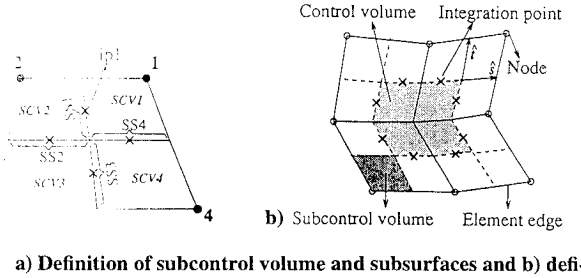

Fig. 2 a) Definition of subcontrol volume and subsurfaces and b) definition of control volume.

Discretization of the Governing Equations

The Navier–Stokes equations for two-dimensional laminar flow are given by

$$\frac{\partial \hat{Q}}{\partial t} + \frac{\partial \hat{E}}{\partial x} + \frac{\partial \hat{F}}{\partial y} = \frac{\partial \hat{G}}{\partial x} + \frac{\partial \hat{H}}{\partial y} \tag{4}$$

where $\hat{Q} = (\rho, \rho u, \rho v, \rho e)^T$, $e = C_v t + (1/2)(u^2 + v^2)$, $\hat{G}$ and $\hat{H}$ include components of stress tensor and heat flux vector, and the convection flux vectors are

$$\hat{E} = \begin{bmatrix} \rho u \\ (\rho u)u + p \\ (\rho u)v \\ (\rho u)h \end{bmatrix} \qquad \hat{F} = \begin{bmatrix} \rho v \\ (\rho v)u \\ (\rho v)v + p \\ (\rho v)h \end{bmatrix} \tag{5}$$

in which $h = C_p t + (1/2)(u^2 + v^2)$. Equation (4) is integrated over each of the SCVs within the element to form the SCV balance equations that together make the elemental matrix equation.

Using a lumped approach, the volume integral of $\partial \hat{Q}/\partial t$ is approximated by its value at the associated SCV node, i.e., $\partial \hat{Q}_i/\partial t$, multiplied by the SCV area. The time derivative, then, is modeled using a backward difference in time. To represent $\hat{Q}_i$ its first term, i.e., density, is substituted from the equation of state and is linearized with respect to P and T; other terms of $\hat{Q}_i$ are linearized with respect to density. The total energy e is linearized with respect to velocity components U and V. Using the divergence theorem, volume integrals of the space derivatives become surface integrals that are evaluated over the SCV surface. As seen in Fig. 2, only intra-element surfaces of SCVs surrounding a node become a part of the control-volume surface for the respective node. Therefore, within an element, integrals are only evaluated over the intra-element surfaces, called subsurfaces (SS), as shown in Fig. 2a. Furthermore, the integral argument, i.e., $\hat{E}$, $\hat{F}$, $\hat{G}$, or $\hat{H}$, is approximated by its average value over the subsurface, evaluated at the midpoint location called an integration point.

The final step is to evaluate the diffusion and convection flux vectors at the integration points. For diffusion flux vectors $\hat{G}$ and $\hat{H}$, bilinear interpolation [Eqs. (1) and (2)] is used to directly evaluate the stress tensor and heat flux vector components. For convection flux vectors, the momentum and energy fluxes are linearized with respect to mass fluxes (ρu) and (ρv). Pressure is related to its nodal values using bilinear interpolation. The velocity components in h are also related to the nodal values using bilinear interpolation. It remains to describe the integration point values of ρu and ρv in the continuity equation and the convected quantities u, v, and t (within h) in the momentum and energy conservation equations in terms of nodal variables U, V, P, and T. This is discussed next.

Pressure-Based Method for Compressible Flow

As mentioned earlier, the continuity equation is treated as a constraint equation for pressure. In compressible flow, where density in addition to velocity is influenced by pressure, the continuity equation constrains pressure from two sources: the pressure/velocity coupling that is crucial in the incompressible regime to resolve the checkerboard problem[13] and the pressure/density coupling that is important in high-speed flow. A suitable linearization of mass fluxes in the continuity equation, therefore, is one that correctly handles this dual role of pressure in compressible flow. This is achieved by a linearization with respect to density and velocity[15]; therefore

$$\rho u = \bar{\rho}u + \rho\bar{u} - \bar{\rho}\bar{u} \tag{6}$$

$$\rho v = \bar{\rho}v + \rho\bar{v} - \bar{\rho}\bar{v} \tag{7}$$

This linearization captures changes of both quantities in each iteration. In the incompressible regime, where $\rho \approx \bar{\rho}$, the second and third terms in Eqs. (6) and (7) cancel. In this case, the effect of pressure gradient, that appears through the integration-point velocities in the first terms, is constrained by the continuity equation. As the compressibility of the flow becomes effective and $\rho \approx \bar{\rho}$ is no longer valid, the influence of pressure on the integration-point

density, via the equation of state, is represented through the second terms. Therefore the continuity equation constrains pressure from both sources.

Having introduced the linearization of mass fluxes, we need to relate integration-point density and velocities to nodal variables in a manner that reflects the coupling associated with them. To deal with the transport nature of density in compressible flow the following profile is used to represent the integration-point density:

$$\rho_{ip} = \rho_{up} + (\overline{\Delta\rho})_{ip} \tag{8}$$

in which substitution of ρ_{up} from the equation of state, i.e.,

$$\rho_{up} = \left(\frac{P_{up}}{RT_{up}}\right) \tag{9}$$

results in a larger influence of the upstream pressure in highly compressible regions. There are two ways to evaluate $(\overline{\Delta\rho})_{ip}$; one is more appropriate for very low Mach number flow, whereas the other is suitable for high-speed flow. For low-Mach-number flow where the bilinear interpolation can be used to evaluate density at the integration point, we have

$$(\overline{\Delta\rho})_{ip} = \sum_{i=1}^{4} N_i(\hat{s}, \hat{t})|_{ip}\bar{\rho}_i - \bar{\rho}_{up} \tag{10}$$

For high-speed flow if $(\overline{\Delta\rho})_{ip}$ is given by

$$(\overline{\Delta\rho})_{ip} = \left(\frac{\overline{\partial\rho}}{\partial s}\right)_{ip} \Delta S \tag{11}$$

then the value of $\partial\rho/\partial s$ can be found from the differential form of the continuity equation, which can be viewed as a transport equation for density in high-speed flow. With the convection term written in the streamwise direction, the continuity equation is rearranged to obtain $\partial\rho/\partial s$ as

$$\frac{\partial\rho}{\partial s} = -\frac{1}{q}\left(\frac{\partial\rho}{\partial t} + \rho\nabla\cdot\boldsymbol{V}\right) \tag{12}$$

Using lagged values from the previous iteration, the right-hand side of Eq. (12) is approximated algebraically, at the integration point, and is substituted into Eq. (11). The location of the upstream point and the value of ΔS will be introduced in the next section.

Equation (11) is used to calculate $(\overline{\Delta\rho})_{ip}$, except for the fully subsonic flows where Eq. (10) is used. However, the dramatic change in $(\overline{\Delta\rho})_{ip}$ across discontinuities, such as shock waves, causes serious instabilities in the solution. To smooth the value of $(\overline{\Delta\rho})_{ip}$, when density oscillations occur, an absolute harmonic interpolation[24] (AHI) is implemented to calculate $(\overline{\Delta\rho})_{ip}$ from its element-nodal values, i.e., from $(\overline{\Delta\rho})_j$ where $j = 1, 4$. The implemented AHI is a two-dimensional version of its one-dimensional form, given in Ref. 25. The integration-point velocities u and v in the mass fluxes ρu and ρv, called the mass conserving or convecting velocities, will be described shortly.

Convected Quantities

Different approaches have been taken to evaluate the convected quantity ϕ at the integration points; ϕ can represent convected quantities u, v, and t. These include the robust but first-order-accurate upwind differencing scheme (UDS), and the second-order accurate central differencing scheme (CDS).[13]

The equation that contains the physics of the problem associated with the convected quantity is given by

$$\rho\frac{\partial\phi}{\partial t} + \rho q\frac{\partial\phi}{\partial s} - \Gamma\nabla^2\phi = S_\phi \tag{13}$$

in which the convection term is represented in the streamwise direction and $q = \sqrt{u^2 + v^2}$. In this study the method of Ref. 19 is adopted to determine the convected quantity ϕ at the integration points. Rather than assuming a profile for ϕ explicitly, the method

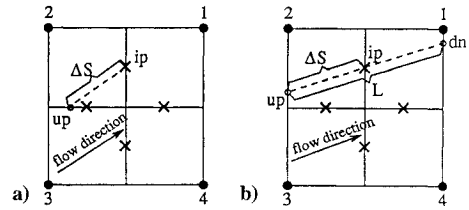

Fig. 3 Skewed upwinding.

derives such a profile implicitly, by algebraically approximating all of the terms in Eq. (13), at the integration point. The value of ϕ_{ip}, then, is obtained through rearrangement of the resulting algebraic equation. In this approach, all terms in Eq. (13) will have an implicit influence on the value of ϕ_{ip}. Since the convection term is upwinded in the streamwise direction, ϕ_{ip} becomes equal to its upstream value ϕ_{up} in a highly convecting flow. The upstream location is obtained by intersecting the upstream flow direction with the first quadrant edge, as shown in Fig. 3a. Depending on the upstream location, the value of ϕ_{up}, then, is interpolated between two integration-point values, between an integration-point and two nodal values, or between two nodal values. The latter case is shown in Fig. 3b. More details about implementation can be found in Ref. 19. For more information regarding different treatments of the convected quantities refer to Ref. 26.

Convecting Velocities

As mentioned earlier, the integration-point velocities in the mass fluxes ρu and ρv are called convecting velocities and hereafter will be denoted by a hat, i.e., $\hat{u}$ and $\hat{v}$. These are the velocities that import and export the convected quantities u, v, and t through the control-volume surface. The convected quantity at the integration point, described in the previous section, is related to the element-nodal variables in a manner that reflects the transport nature of that quantity. The primary aim in finding a formulation for the convecting velocity, however, is to include the coupling between pressure and velocity such that the substitution of this formulation into the mass conservation equation leads to a set of equations that results in oscillation-free pressure and velocity fields. To achieve this, the momentum equation that includes the influence of pressure on velocity is used first to obtain a formulation for the convecting velocity. This stage is performed quite similar to the procedure described in the previous section for obtaining a convected quantity (velocity here). For simplicity, consider the u-momentum equation for steady incompressible Euler flow, given by

$$\rho q\frac{\partial u}{\partial s} + \frac{\partial p}{\partial x} = 0 \tag{14}$$

and the regular element shown in Fig. 3b. To obtain a formulation for the convecting velocity $\hat{u}_{ip}$, Eq. (14) is approximated algebraically at ip, as

$$\rho q_{ip}\left(\frac{\hat{u}_{ip} - u_{up}}{\Delta S}\right) + \left(\frac{\partial p}{\partial x}\right)^{l}_{ip} = 0 \tag{15}$$

where u_{up} in the convection term, upwinded in the flow direction, is interpolated between U_2 and U_3. After rearrangement we get

$$\hat{u}_{ip} = u_{up} - \frac{\Delta S}{\rho q_{ip}}\left(\frac{\partial p}{\partial x}\right)^{l}_{ip} \tag{16}$$

and by a similar procedure

$$\hat{v}_{ip} = v_{up} - \frac{\Delta S}{\rho q_{ip}}\left(\frac{\partial p}{\partial y}\right)^{l}_{ip} \tag{17}$$

Up to this stage we have precisely followed the procedure applied for obtaining convected velocities. Therefore, Eqs. (16) and (17) describe components of convected velocities as well as components of convecting velocities, for now. Equations (16) and (17), which express how the pressure variation within the element affects

integration-point velocities, are obtained using only the momentum equations. The continuity equation is not used, and therefore no information about the continuity constraint within the element is directly included in these equations. With such convecting and convected velocities the resulting velocity field reflects a one-way function of the pressure field; i.e., there would be no feedback from the continuity constraint felt by the integration-point velocities.

Using Eqs. (16) and (17) to define both the convecting and convected velocities, solutions of simple one-dimensional[27] and two-dimensional[21] Euler flows have demonstrated that unique checkerboard pressure and velocity fields can be formed in which momentum equation errors defined as

$$\dot{\varepsilon}_{x_{ip}} = \left[\rho q \frac{\partial u}{\partial s} + \left(\frac{\partial p}{\partial x} \right)^{l} \right]_{ip} \tag{18}$$

$$\dot{\varepsilon}_{y_{ip}} = \left[\rho q \frac{\partial v}{\partial s} + \left(\frac{\partial p}{\partial y} \right)^{l} \right]_{ip} \tag{19}$$

are equal to zero but, surprisingly, a continuity equation error defined as

$$\ddot{\varepsilon}_{ip} = \rho \left(\frac{\partial u}{\partial x} + \frac{\partial v}{\partial y} \right)^{l}_{ip} \tag{20}$$

would not be zero. This characteristic of the solution, although for simple cases, leads us to conclude that such a checkerboard solution most probably is the outcome of obtaining $\hat{u}_{ip}$ and $\hat{v}_{ip}$ without any reference to the continuity equation. This drawback can be modified by including the effect of the continuity equation error in Eqs. (16) and (17). Considering $\hat{u}_{ip}$, an implementation of such an approach would be first to scale $\ddot{\varepsilon}_{ip}$ by u and subtract it from the left-hand side of Eq. (14), i.e.,

$$\left(\rho q \frac{\partial u}{\partial s} + \frac{\partial p}{\partial x} \right) - u \ddot{\varepsilon}_{ip} = 0 \tag{21}$$

and second to implement the same procedure as applied to obtain Eq. (16) to Eq. (21) to get the new $\hat{u}_{ip}$ as

$$\hat{u}_{ip} = u_{up} - \frac{\Delta S}{\rho q_{ip}} \left[\left(\frac{\partial p}{\partial x} \right)^{l}_{ip} - u \ddot{\varepsilon}_{ip} \right] \tag{22}$$

where $\ddot{\varepsilon}_{ip}$ is defined by Eq. (20). Our experience shows that it is very effective if $u\ddot{\varepsilon}_{ip}$ is rearranged in the flow direction as

$$u \ddot{\varepsilon}_{ip} = \rho q_{ip} \left(\frac{\partial u}{\partial s} \right)_{ip} - \rho \left(v \frac{\partial u}{\partial y} - u \frac{\partial v}{\partial y} \right)^{l}_{ip} \tag{23}$$

with $(\partial u/\partial s)_{ip}$ modeled as

$$\left(\frac{\partial u}{\partial s} \right)_{ip} = \frac{u_{dn} - u_{up}}{L} \tag{24}$$

After substitution of $u\ddot{\varepsilon}_{ip}$ from Eq. (23) into Eq. (22) and rearrangement, $\hat{u}_{ip}$ is obtained as

$$\hat{u}_{ip} = \tilde{u}_{ip} - \frac{\Delta S}{\rho q_{ip}} \left(\rho v \frac{\partial u}{\partial y} - \rho u \frac{\partial v}{\partial y} + \frac{\partial p}{\partial x} \right)^{l}_{ip} \tag{25}$$

where

$$\tilde{u}_{ip} = \frac{\Delta S}{L} u_{dn} + \left(1 - \frac{\Delta S}{L} \right) u_{up} \tag{26}$$

and u_{dn} and u_{up} are interpolated between the two nodal velocities U_1, U_4 and U_2, U_3, respectively. Combining Eqs. (18), (23), and (25), $\hat{u}_{ip}$ can also be represented as

$$\hat{u}_{ip} = \tilde{u}_{ip} - \frac{\Delta S}{\rho q_{ip}} \left(\dot{\varepsilon}_{x_{ip}} - u \ddot{\varepsilon}_{ip} \right) \tag{27}$$

which exhibits how the continuity equation error and the corresponding momentum equation error appear in the convecting velocity. The same procedure can be applied to obtain an equation similar to Eq. (25) for $\hat{v}_{ip}$, as

$$\hat{v}_{ip} = \tilde{v}_{ip} - \frac{\Delta S}{\rho \tilde{q}_{ip}} \left(\rho u \frac{\partial v}{\partial x} - \rho v \frac{\partial u}{\partial x} + \frac{\partial p}{\partial y} \right)^{l}_{ip} \tag{28}$$

where a definition similar to Eq. (26) is introduced for $\tilde{v}_{ip}$. The unique checkerboard pressure and velocity fields, mentioned earlier, are eliminated with the present formulation; see Refs. 27 and 21.

To have the preceding procedure valid for all flow speed calculations, the method should be modified to include compressibility effects. Other than that ρ_{ip} is no longer constant, the main adjustment is the inclusion of density derivatives in $\ddot{\varepsilon}_{ip}$, in addition to velocity derivatives; $\ddot{\varepsilon}_{ip}$ then becomes

$$\ddot{\varepsilon}_{ip} = \rho_{ip} \left(\frac{\partial u}{\partial x} + \frac{\partial v}{\partial y} \right)^{l}_{ip} + \left(u \frac{\partial \rho}{\partial x} + v \frac{\partial \rho}{\partial y} + \frac{\partial \rho}{\partial t} \right)_{ip} \tag{29}$$

in which the second bracket is approximated using a backward difference for the transient term and bilinear interpolation for the space derivatives. In transonic flow special treatment of density space derivatives reduces under/overshoots in the vicinity of shock waves. In such cases space derivatives are rearranged to form a convection term for density, and upwinding in the flow direction is applied to approximate this term; see Ref. 24. Finally, in a viscous transient flow, diffusion and transient terms are included in Eq. (14) and/or the first bracket of Eq. (21). In terms of computational effort, calculation of the proposed convecting velocity is economical since it has only $u\ddot{\varepsilon}_{ip}$ (or $v\ddot{\varepsilon}_{ip}$) extra to the convected velocity formulation.

The approximation made to the convected quantities is identical to that in the FIELDS[19] method. The convecting velocity, however, contains additional terms presented earlier. The order of error, due to algebraic approximations applied to these terms, is not lower than that produced by approximations made to other terms in the main equation, e.g., Eq. (21). As a result, the second-order accuracy of the FIELDS method, demonstrated by the grid convergence study in Ref. 28, applies to the present method. For more details see Ref. 24.

Numerical Results

The results presented in this section will demonstrate the validity of the present method for solving viscous/inviscid fluid flow problems ranging from very low Mach number to supersonic. The test cases include driven cavity flow, subsonic, transonic, and supersonic flows in a duct with a bump, and supersonic flow in a duct with a 21.57-deg ramp. In the cases the accuracy of the results is assessed by comparing the results with other numerical results available in the literature and an exact solution for the last case. The steady-state solution is obtained by marching in time with large time steps (relative to the time scale of the problem). In each time step the linearized system of equations is solved once, using a direct sparse solver. Marching in time was performed to reduce ϵ, the normalized L_2 norm of the error, below 1.0×10^{-3}. All test problems have been computed on a SPARCstation 2. Continued marching resulted in monotonic reduction in the L_2 norm to less than 10^{-10}.

Boundary Conditions

In this section the boundary conditions are briefly outlined.

Wall Boundary

For viscous flows, a no-slip boundary condition is applied along the solid wall by setting velocity components equal to zero. For inviscid flows, where the tangency condition is applied along the wall, the tangential momentum equation is conserved, and the component of velocity normal to the wall is set equal to zero. In both viscous and inviscid flows the mass conservation equation is closed using zero mass flux at the wall. For nonisothermal flow, the energy equation is closed using known conduction and zero convection energy fluxes at the solid wall.

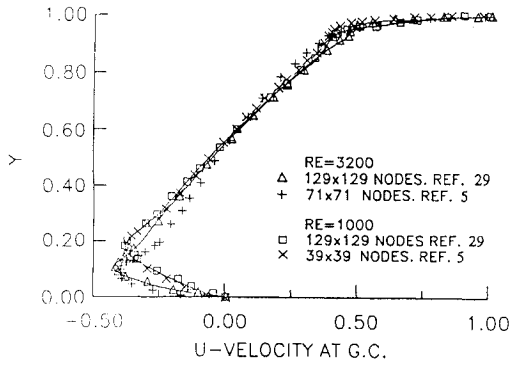

Fig. 4 The u-velocity component along the vertical centerline of the driven cavity for $Re = 1 \times 10^3$ and 3.2×10^3.

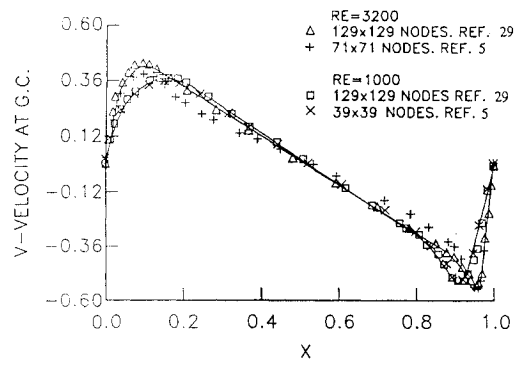

Fig. 5 The v-velocity component along the horizontal centerline of the driven cavity for $Re = 1 \times 10^3$ and 3.2×10^3.

Inlet Boundary

For subsonic flows, velocity components and temperature are specified, and the mass conservation equation is closed by representing the inlet mass flux in terms of nodal variables. For supersonic flows, all variables are specified.

Outlet Boundary

For subsonic flows, the static pressure and flow direction are specified, temperature is extrapolated in the flow direction from the interior points, and the mass conservation equation is treated as was handled for subsonic flows at the inlet. For supersonic flows, all variables are extrapolated in the flow direction from the interior points, identified as B.C.I. The other option, identified as B.C.II, is to close the mass and momentum conservation equations by representing outlet convection fluxes in terms of nodal variables.

Driven Cavity Flow

The present method was applied to solve the two-dimensional laminar flow in a square cavity of 1.0×1.0 for two Reynolds numbers of 1×10^3 and 3.2×10^3 under isothermal conditions; $T = 300$ K. This problem has served as a standard test case for incompressible viscous calculation, despite the singularities at two of its corners. All of the walls are fixed except the top wall, which moves with a constant velocity of 1.0. This results in the isothermal Mach number, $u/\sqrt{RT}$, being below 3.41×10^{-3} in the solution domain. Calculations are carried out on a grid with 51×51 equally spaced nodes and a regular structure.

The u-velocity component along the vertical centerline and the v-velocity component along the horizontal centerline for these two Reynolds numbers are shown in Figs. 4 and 5. The present results (solid line) are compared with those of Refs. 5 and 29. Excellent agreement is seen with Ref. 29, especially for $Re = 3.2 \times 10^3$ where the 51×51 grid is relatively coarse. Starting from zero velocity initial conditions, 11 and 15 large time steps ($\Delta t = 10^{10}$ s) were taken to meet the target ϵ, for cases $Re = 1 \times 10^3$ and 3.2×10^3, respectively. The CPU time per iteration was about 382 s. In comparison to the results of Ref. 21, for a true incompressible code, the same number of iterations was required for both $Re = 1 \times 10^3$ and 3.2×10^3. Given that the same time steps and a direct solver are used in both studies, the preceding comparison demonstrates that the compressibility effect does not impose any time step limitation on the solution procedure at very low Mach numbers. The streamline patterns for $Re = 1 \times 10^3$ and 3.2×10^3 are shown in Fig. 6.

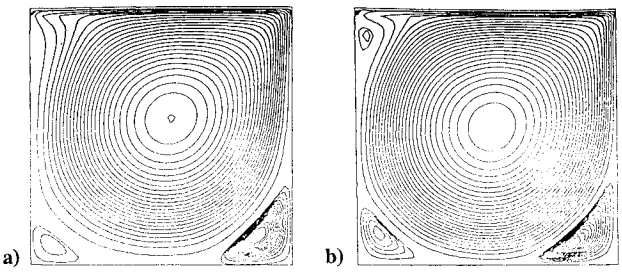

Fig. 6 Streamline pattern of the driven cavity flow on a 51×51 grid: a) $Re = 1 \times 10^3$ and b) $Re = 3.2 \times 10^3$.

Flow in a Channel with a Bump

Inviscid flow in a channel with a bump on the middle of its lower wall is solved for the flow regimes of subsonic, transonic, and supersonic. This problem is well suited for code development and testing. The problem symmetry and geometric simplicity help the interpretation of the results. The length of the channel is three times the chord length of the bump. The upper and the lower walls are located a chord length from each other. The thickness of the bump is equal to 10% of its chord for the subsonic and transonic flows and is equal to 4% of its chord for the supersonic flow. A 65×17 nonuniform grid, used for subsonic and transonic calculations, is shown in Fig. 7a.

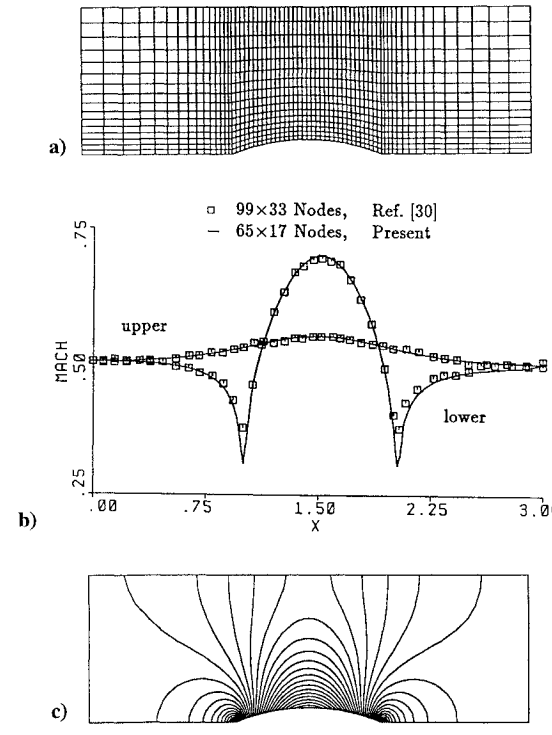

Fig. 7 Subsonic solution for flow in channel with $M_{in} = 0.5$: a) grid structure, b) Mach number distributions, and c) isobar plot.

The grid points are stretched in the bump region and near the lower wall. For the supersonic calculation, a 60×20 nonuniform grid is used. The grid points are stretched in and after the bump region and near the lower and the upper walls. For all three speeds, the energy conservation equation is closed using zero energy fluxes at the solid walls. Note that, in representing results from other sources, the number of symbols does not indicate the number of nodes, necessarily. In all three cases, initial conditions of temperature and pressure are $T = T_{in} = 300$ K and $P = P_{in} = 8.61 \times 10^4$ N/m^2, respectively.

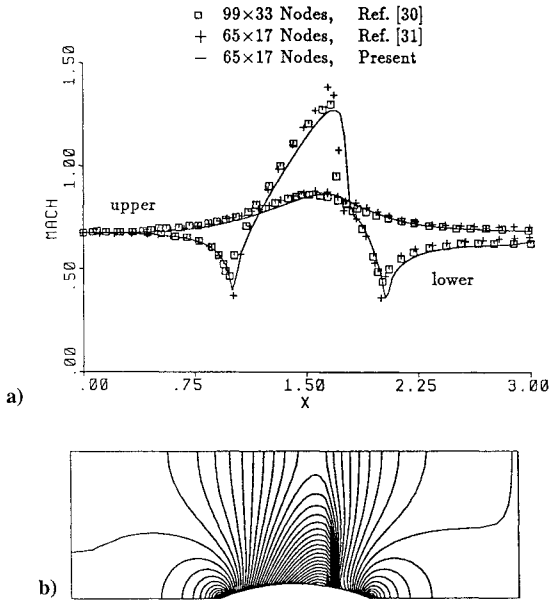

Fig. 8 Transonic solution for flow in channel with $M_{in} = 0.675$: a) Mach number distributions and b) isobar plot.

Results of Subsonic Flow

With the inlet Mach number of 0.5 the inviscid flow in the channel is subsonic and is symmetric about the middle of the bump. The Mach number distributions along the lower and the upper walls are compared with Ref. 30 in Fig. 7b. The agreement is excellent, although a lower Mach number is predicted at the bump edges. A little asymmetry is seen on the lower wall, which is due to the numerical implementation of the tangency boundary condition. The isobar plot for this case is presented in Fig. 7c. Initial conditions of velocity were $u = v = 0$, and eight time steps of $\Delta t = 1.0$ s were taken to meet the target ϵ. The CPU time per iteration was about 48 s.

Results of Transonic Flow

In this case the inlet Mach number is 0.675, which creates a transonic flow in the channel. The Mach number distributions along the lower and the upper walls are presented in Fig. 8a. We have compared the present results with the results of Refs. 30 and 31. The overall agreement is very good. The shock wave is captured within four nodes, and its strength is about the same as that of Ref. 30. However, the location of the shock is predicted a bit downstream. This can be improved by grid refinement in this region. The sonic line impinging on the aft bump is at a distance of 75% chord length from the leading edge. This distance is predicted to be 72 and 73% chord length by Refs. 31 and 32, respectively. Ni[31] predicted a stronger shock wave as is shown in Fig. 8a; also see Refs. 32 and 33. The isobar plot is presented in Fig. 8b. The initial conditions of velocity are similar to those in subsonic flow. Twenty five time steps of $\Delta t = 1.0$ s were taken to meet the target ϵ. The CPU time per iteration was about 49 s.

Results of Supersonic Flow

Figure 9 presents results of the supersonic flow in a 4% thick arc bump channel with the inlet Mach number of 1.65. The oblique shock wave leaving the trailing edge intersects with the reflection of the oblique shock wave leaving the leading edge. After intersection both shocks leave the solution domain. This test problem contains a complex supersonic flow and is used to check the robustness of code. The isobar plot, shown in Figs. 9c and 9d, demonstrates the complexity of the flow. The Mach number distributions along the lower and upper walls are compared with the results of Ref. 30 in Fig. 9b. The agreement is exceptionally good at both the lower and the upper walls. At the upper wall a stronger reflection is predicted by the present method.

Figures 9c and 9d are the isobar plots with two different outlet boundary conditions B.C.I and B.C.II. With the B.C.I where the variables are extrapolated at the outlet, both oblique shock waves leaving

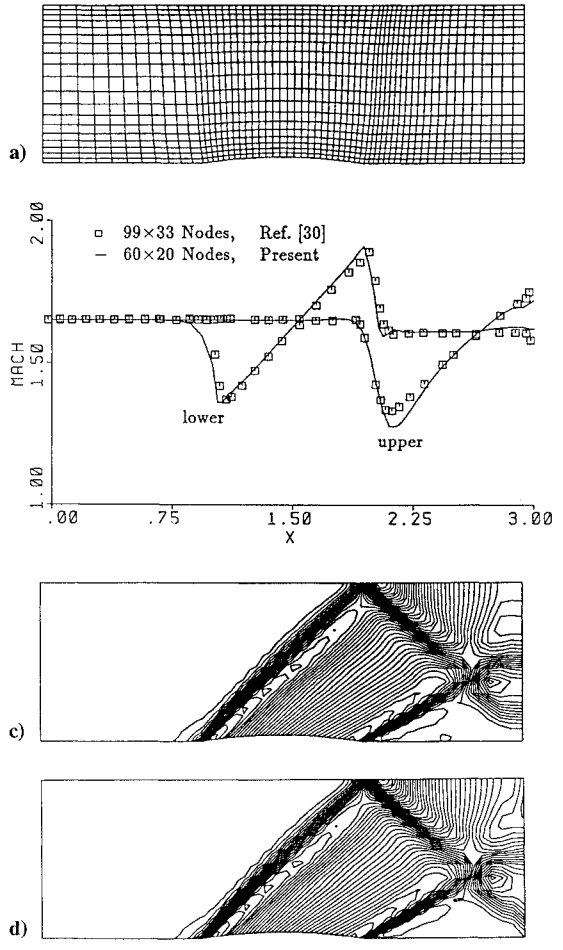

Fig. 9 Supersonic solution for flow in channel with $M_{in} = 1.65$: a) grid structure, b) Mach number distributions, c) isobar plot with B.C.I, and d) isobar plot with B.C.II.

the domain lose their correct angle at the outlet. This situation is improved by implementing B.C.II, which closes the flow equations at the outlet. The lower shock wave is turned completely to its correct angle. Since the grid is very coarse in the middle of the outlet, the upper shock wave is not improved much. To speed up convergence, 10 time steps of $\Delta t = 2 \times 10^{-4}$ s and 18 time steps of $\Delta t = 2 \times 10^{-2}$ s have been taken from the initial conditions of $u = 500.0$ m/s and $v = 0.0$ m/s. The CPU time per iteration was about 64 s.

Supersonic Flow in a Duct with a Ramp

This case is chosen to demonstrate the ability of the method for the solution of supersonic flow encountering an oblique shock wave. Since the exact solution is available, comparison can be made to present the accuracy of the method. Supersonic flow with a Mach number of 2.5 enters a duct whose length and width are 1.3 and 1.2 m, respectively, in the x and y directions. The lower wall has a 21.57-deg ramp. The distance between the inlet and the leading edge of the ramp is 0.3 m. The ramp creates a 45-deg oblique shock with the strength of $M_2/M_1 = 0.628$, $P_2/P_1 = 3.497$, and $T_2/T_1 = 1.508$.

A 45×30 uniform grid, Fig. 10a, is used for the computation. We have compared the Mach number distribution along the $y = 0.75$ m line with the exact solution in Fig. 10b. The strength of the oblique shock, captured within six nodes, is predicted very accurately. Since the shock wave intersects the $y = 0.75$ line obliquely, the result is smeared over more nodes. Figure 10c presents the Mach number along a line normal to the oblique shock, i.e., with -45 deg. As is seen, the shock is smeared over 3–4 nodes. Starting from initial conditions of $u = 500.0$ m/s and $v = 0.0$ m/s, the following procedure was used to speed up the convergence: 10 time steps of $\Delta t = 10^{-4}$ s, 10 time steps of $\Delta t = 10^{-3}$ s, and 9 time steps of $\Delta t = 10^{-2}$ s. The CPU time per iteration was about 126 s. Based on the speed of sound at the outlet and the smallest element size,

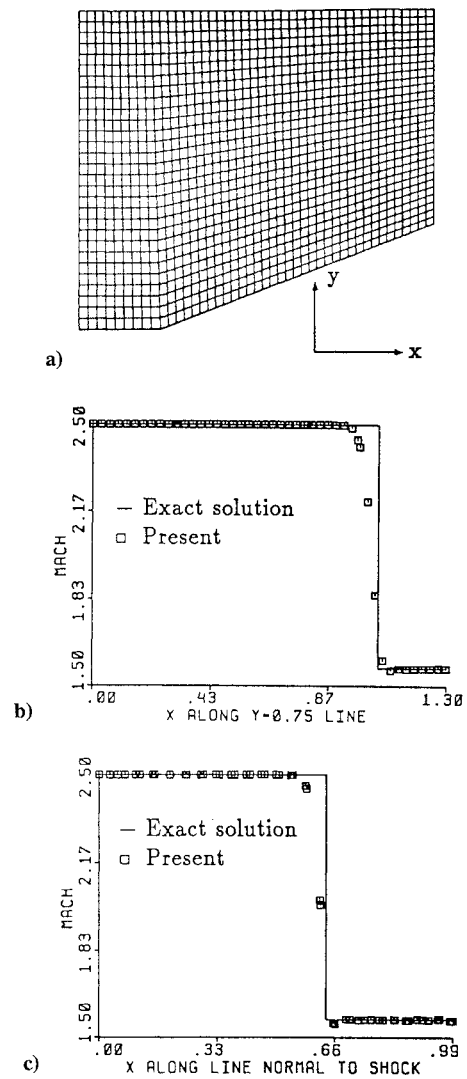

Fig. 10 Supersonic flow in channel with a ramp at M_{in} = 2.5: a) the grid, b) Mach number along y = 0.75 line, and c) Mach number along a line normal to the oblique.

the Courant–Friedrichs–Lewy (CFL) numbers for these three stages are 1.59, 15.9, and 159.

As a transient test, we also solved the unsteady flow over a circular cylinder at a Reynolds number of 2×10^2 (based on diameter) under isothermal conditions. The computation was performed on an O-type 60×81 grid, with its outer boundary located 20 diameters from the cylinder center. Details are discussed in Ref. 24. The Strouhal number based on the streamline patterns was calculated to be 0.18. This result is close to 0.19, reported by Roshko[34] from his experiments. Considering that the Strouhal number was calculated based on the similarity of the streamline patterns during cycles and was calculated after the first periodic cycle on the coarse grid used, its value is very well predicted.

With respect to memory allocation, it is noted that no measures were implemented to optimize or minimize these requirements. However, for the sample case of driven cavity problem, which requires 2601 nodes and 10,000 integration points, 10 real words were stored per node, not including the usual element bookkeeping storage. In addition, 10 real words were stored per integration points, although this is not absolutely necessary and is a consideration in balance between CPU time and storage. It is noted that the preceding figures do not include requirements for the solver and its associated matrix structure.

Conclusions

The objective of this study was to develop a method for solving flow at all speeds. This objective has been achieved via inclusion of correct pressure/velocity and pressure/density couplings in the scheme. As a result, the present method is capable of preventing oscillations in pressure and velocity in incompressible flow, known as the pressure checkerboard problem, and simulating transonic and highly supersonic flows accurately. The method is implicit, there being no time step limitation due to compressibility at low Mach numbers.

A variety of different test problems has been examined to check the accuracy, capability, and robustness of the method. Test problems cover the range from fully incompressible to Mach 2.5. Results have been compared with other results available in the literature and an exact solution. In all cases the predicted results agreed very well. In transonic and supersonic flows shock waves have been captured quite sharply. The effect of two different boundary conditions at the supersonic outlet was also examined. The method was developed in two dimensions; however, it can be easily extended to three dimensions.

Acknowledgments

The first author would like to express appreciation for the scholarship he received from the Ministry of Culture and Higher Education of Iran. The financial support of the Natural Sciences and Engineering Research Council of Canada is gratefully acknowledged.

References

[1]Turkle, E., "Preconditioned Methods for Solving the Incompressible and Low Speed Compressible Equations," *Journal of Computational Physics*, Vol. 72, No. 2, 1987, pp. 277–298.

[2]Hsu, C. H., Chen, Y. M., and Liu, C. H., "Preconditioned Upwind Methods to Solve Incompressible Navier–Stokes Equations," *AIAA Journal*, Vol. 30, No. 2, 1992, pp. 550–552.

[3]Choi, D., and Merkle, C. L., "Application of a Time-Iterative Scheme to Incompressible Flow," *AIAA Journal*, Vol. 23, No. 10, 1985, pp. 1518–1524.

[4]Choi, Y., and Merkle, C. L., "Time-Derivative Preconditioning for Viscous Flow," AIAA Paper 91-1652, June 1991.

[5]Chen, K. H., and Pletcher, R. H., "Primitive Variable, Strongly Implicit Calculation Procedure for Viscous Flows at All Speeds," *AIAA Journal*, Vol. 29, No. 8, 1991, pp. 1241–1249.

[6]Pletcher, R. H., and Chen, K. H., "On Solving the Compressible Navier–Stokes Equations for Unsteady Flows at Very Low Mach Numbers," AIAA Paper 93-3368, July 1993.

[7]Zienkiewicz, O. C., Lohner, R., Morgan, K., and Peraire, J., "High Speed Compressible Flow and Other Advection Dominated Problems of Fluid Mechanics," *Finite Elements in Fluids*, edited by R. H. Gallagher, G. Garey, J. T. Oden, and O. C. Zienkiewicz, Wiley, New York, 1985, pp. 41–48.

[8]Zienkiewicz, O. C., and Taylor, R. L., *The Finite-Element Method*, Vol. 2, 4th ed., McGraw–Hill, New York, 1989, Chap. 14.

[9]Hughes, T. J. R., "Recent Progress in the Development and Understanding of SUPG Methods with Special Reference to the Compressible Euler and Navier–Stokes Equations," *Finite Elements in Fluids*, Vol. 7, Wiley, Toronto, 1987, pp. 273–287.

[10]Franca, L. P., Harari, I., Hughes, T. J. R., Mallet, M., Shakib, F., Spelce, T. E., Chalot, F., and Tezduyar, T. E., "A Petrov–Galerkin Finite Element Method for the Compressible Euler and Navier–Stokes Equations," *Numerical Methods for Compressible Flows: Finite Difference, Element and Volume Techniques*, American Society of Mechanical Engineers, New York, 1986, pp. 19–43.

[11]Zienkiewicz, O. C., Szmelter, J., and Peraire, J., "Compressible and Incompressible Flow; An Algorithm for All Seasons," *Computer Methods in Applied Mechanics and Engineering*, Vol. 78, No. 1, 1990, pp. 105–121.

[12]Zienkiewicz, O. C., and Wu, J., "A General Explicit or Semi-Explicit Algorithm for Compressible and Incompressible Flows," *International Journal for Numerical Methods in Engineering*, Vol. 35, No. 3, 1992, pp. 457–479.

[13]Patankar, S. V., *Numerical Heat Transfer and Fluid Flow*, Hemisphere, Washington, DC, 1980, Chaps. 5 and 6.

[14]Van Doormaal, J. P., and Raithby, G. D., "An Evaluation of the Segregated Approach for Predicting Incompressible Fluid Flows," American Society of Mechanical Engineers, ASME Paper 85-HT-9, Aug. 1985.

[15]Van Doormaal, J. P., Raithby, G. D., and McDonald, B. H., "The Segregated Approach to Predicting Viscous Compressible Fluid Flows," *Journal of Turbomachinery, ASME*, Vol. 109, No. 2, 1987, pp. 268–277.

[16]Karki, K. C., and Patankar, S. V., "Pressure-Based Calculation Procedure for Viscous Flows at All Speeds in Arbitrary Configurations," *AIAA Journal*, Vol. 27, No. 9, 1989, pp. 1167–1174.

[17]Shyy, W., Chen, M. H., and Sun, C. S., "Pressure-Based Multigrid Algorithm for Flow at All Speeds," *AIAA Journal*, Vol. 30, No. 11, 1992, pp. 2660–2669.

[18]Rhie, C. M., and Chow, W. L., "Numerical Study of the Turbulent Flow Past an Airfoil with Trailing Edge Separation," *AIAA Journal*, Vol. 21, No. 11, 1983, pp. 1525–1532.

[19]Schneider, G. E., and Raw, M. J., "Control-Volume Finite-Element Method for Heat Transfer and Fluid Flow Using Co-Located Variables—1. Computational Procedure," *Numerical Heat Transfer*, Vol. 11, No. 4, 1987, pp. 363–390.

[20]Raw, M. J., Galpin, P. F., and Raithby, G. D., "The Development of an Efficient Turbomachinery CFD Analysis Procedure," AIAA Paper 89-2394, July 1989.

[21]Karimian, S. M. H., and Schneider, G. E., "Numerical Solution of Two-Dimensional Incompressible Navier–Stokes Equations: Treatment of Velocity-Pressure Coupling," AIAA Paper 94-2359, June 1994.

[22]Rhie, C. M., "Pressure-Based Navier–Stokes Solver Using the Multigrid Method," *AIAA Journal*, Vol. 27, No. 8, 1989, pp. 1017–1018.

[23]Karimian, S. M. H., and Schneider, G. E., "Pressure-Based Computational Method for Compressible and Incompressible Flows," *Journal of Thermophysics and Heat Transfer*, Vol. 8, No. 2, 1994, pp. 267–274.

[24]Karimian, S. M. H., "Pressure-Based Control-Volume Finite-Element Method for Flow at All Speeds," Ph.D. Dissertation, Univ. of Waterloo, Waterloo, Ontario, Canada, 1994.

[25]Anon., "Theory Documentation of TASCFLOW Code," Version 2.2, Advanced Scientific Computing, Ltd., Waterloo, Ontario, Canada, Oct. 1992.

[26]Van Doormaal, J. P., Turan, A., and Raithby, G. D., "Evaluation of New Techniques for the Calculation of Internal Recirculating Flows," AIAA Paper 87-0059, Jan. 1987.

[27]Schneider, G. E., and Karimian, S. M. H., "Advances in Control-Volume Based Finite-Element Methods for Compressible Flows," *Computational Mechanics*, Vol. 14, No. 5, 1994, pp. 431–446.

[28]Schneider, G. E., and Raw, M. J., "Control-Volume Finite-Element Method for Heat Transfer and Fluid Flow Using Co-Located Variables—2. Application and Validation," *Numerical Heat Transfer*, Vol. 11, No. 4, 1987, pp. 391–400.

[29]Ghia, U., Ghia, K. N., and Shin, C. T., "High-Re Solutions for Incompressible Flow Using the Navier–Stokes Equations and a Multigrid Method," *Journal of Computational Physics*, Vol. 48, No. 3, 1982, pp. 387–411.

[30]Eidlman, S., Colella, P., and Shreeve, R. P., "Application of the Godonov Method and Its Second-Order Extension to Cascade Flow Modeling," *AIAA Journal*, Vol. 22, No. 11, 1984, pp. 1609–1615.

[31]Ni, R. H., "A Multiple-Grid Scheme for Solving the Euler Equations," *AIAA Journal*, Vol. 20, No. 11, 1982, pp. 1565–1571.

[32]Jorgenson, P. C. E., and Pletcher, R. H., "An Implicit Numerical Scheme for the Simulation of Internal Viscous Flows on Unstructured Grids," AIAA Paper 94-0306, Jan. 1994.

[33]Chima, R. V., and Johnson, G. M., "Efficient Solution of the Euler and Navier–Stokes Equations with a Vectorized Multiple-Grid Algorithm," *AIAA Journal*, Vol. 23, No. 1, 1985, pp. 23–32.

[34]Roshko, A., "On the Development of Turbulent Wakes from Vortex Streets," NACA 1191, 1954.